J. Fluid Mech. (1988), *vol.* 186, *pp.* 419–444
Printed in Great Britain

Linear internal waves generated by density and velocity perturbations in a linearly stratified fluid

By JAMES C. S. MENG

Gould Defense Systems, Inc., Ocean Systems Division, One Corporate Place, Newport Corporate Park, Middletown, RI 02840, USA

AND JAMES W. ROTTMAN

Department of Marine, Earth & Atmospheric Sciences, North Carolina State University, Raleigh, NC 27695, USA

(Received 13 June 1985 and in revised form 3 July 1987)

A generalized theoretical analysis and finite-difference solutions of the Navier–Stokes equations of the initial-value problem are applied to obtain the linear internal wave fields generated by a density perturbation and two rotational velocity perturbations in an inviscid linearly stratified fluid. The velocity perturbations are those due to an axisymmetric swirl and a vortex pair. Solutions obtained correspond to the strong stratification limit.

The theoretical results of the rotational perturbation cases show an oscillating non-propagating disturbance, which is absent in the density-perturbation case. The swirl-flow solution shows an oscillatory behaviour in both the angular momentum deposited in the fluid and in the torque exerted by the external gravitational force field. The vortex-flow solution shows a vertical ray pattern.

The equi-partitioning of energy is reached at about 0.4 of a Brunt–Väisälä (B.V.) period. The potential energy–kinetic energy conversion, or vice versa, takes place between 0.15 and 0.3 B.V. periods.

1. Introduction

The wake generated by a self-propelled submerged body in a density stratified fluid has been a subject of intense study in the past two decades. In general, the phenomenon includes two major physical elements; the internal waves and turbulent wakes. For the internal waves, in particular, that generated by the collapse of a mixed wake in an incompressible, stratified fluid, the theoretical work of Mei (1969), Miles (1971), Hartman & Lewis (1972) and the experimental studies by Schooley & Hughes (1972) and Wu (1969) have all contributed to the present understanding of the problem. Schooley & Hughes also gave a linear theoretical analysis using the normal mode theory in a finite vertical domain, and obtained good agreement with Wu's (1969) experimental data. Wessel (1969) solved numerically the Navier–Stokes equation for the unsteady flow resulting from releasing a square region of fluid that has been mixed uniformly. His result was also in good agreement with Wu's data. In the analysis by Hartman & Lewis (1972) however, an oversimplified initial condition for the density anomaly introduced a mathematical singularity at the boundary of the mixed region. This singularity is removed in our study and the differences are discussed. For the turbulent wake studies, Schooley & Stewart (1963) presented

experimental data on a self-propelled body moving through a density stratified fluid. Janowitz (1968) derived the linear-flow solution far upstream and downstream of a body moving very slowly through a stratified viscous fluid. Peyret (1976) did a numerical study of the unsteady laminar flow due to the penetration of a horizontal jet of constant density into a stratified fluid. Lin & Pao (1979) gave an extensive experimental data base on the turbulent wakes in a stratified fluid.

None of these studies provided the solutions of internal waves generated by rotational velocity perturbations which are an integral part of the wake disturbances, and will be our focus here. In particular, the internal wave fields generated by a swirl motion and a vortex pair have not been studied. These two rotational flows are chosen for this study not only because of their practical occurrence in ocean but also the interesting contrast in physical nature and the resulting internal waves. For example, a swirl velocity profile can exist alone, while vortex must appear in pairs; a swirl can generate torque, but a vortex pair cannot; a vortex pair can generate lift, a swirl cannot; a swirl produces an antisymmetric internal wave field while a vortex pair produces a symmetric one.

Any rotational object can generate a swirling flow field, for example by a propeller. In an unstratified fluid the swirl Froude number $F_{\text{swirl}} = \infty$, a swirling flow decays primarily due to turbulent diffusion. In a stably stratified fluid, eventually part of the swirl energy will be converted into internal waves. As the density stratification increases, F_{swirl} approaches 1, most of the kinetic energy will be converted into propagating internal wave energy. It is the solutions in this strongly stratified limit that we are interested in here. For the vortex case the effects of density stratification on the trailing vortices behind an aircraft have been studied by Saffman (1972), numerically simulated by Brown & Kirkman (1974) and by Hill (1975), and experimentally by Tombach (1974). All these studies correspond to the strong nonlinear, or weak density stratification case, i.e. the vortex Froude number $F_{\text{vortex}} > 1$. In the ocean, the density stratification is much stronger, and the vortices are weaker because no large lift force is necessary to sustain a level flight, so that it is likely that $F_{\text{vortex}} < 1$. Currently there is no theoretical model to analyse these physical phenomena in the strongly stratified limit.

Owing to the simplicity of the physical problem and the convenience of the theoretical analysis used by Hartman & Lewis, it is desirable to generalize their technique to study the effects of these rotational flows in a linearly stratified fluid. This paper presents a generalization of Hartman & Lewis' analysis. The objective is to establish and illustrate the fundamental differences between the internal wave fields generated by a density perturbation and those generated by rotational velocity perturbations. Solutions are given in closed form for the density deviation ρ' from the ambient density ρ_0, the stream function ψ, and the vorticity Ω. Asymptotic expressions for both the long-time and far-field limits are established.

Due to the linearity of the governing equations, superposition can be used to study a large class of interesting physical problems. For example, the smoothed density perturbation solution can be superposed with the swirl-flow solution to obtain the density anomaly field in a vigorously mixed region, and solution of pairs of vortices can be obtained by superposing vortices spaced apart in any orientation.

In §2 the general mathematical formulation of the problem is described, and the general analytical solution for an arbitrary set of initial conditions is given in closed form. In the remaining sections the general formulation is applied to three particular sets of initial conditions. Each section contains a description of the solution and its

properties, a numerical evaluation of the analytical solution presented in terms of density contour plots, and a comparison of these results with a finite-difference solution of the fully nonlinear Navier–Stokes equations in the Boussinesq approximation. The finite-difference solution is obtained by using a two-dimension unsteady computer code. Such a comparison is valuable in establishing the range of flow parameters over which the linear approximation applied in the linear analytic method is accurate. Section 3 describes the solution for a smoothed version of the density perturbation used by Hartman & Lewis. Namely the singularity at the mixed region boundary in their initial condition is removed. Comparison of this treatment with the original analysis shows a factor of four increase in the internal wave amplitude in the far field. Section 4 describes the solution for the swirl-flow problem. Section 5 dwells on the solution for a single vortex first; then the numerical result for a vortex pair is presented and analysed. Two vortex models were used; the Rankine model and the Lamb model. The former is more widely used, while the latter is theoretically more tractable. Their equivalence in both the near- and far-fields is established and their asymptotic results are shown to be identical. Section 6 summarizes the main results.

2. General mathematical formulation of the problem

2.1. *Analytical method*

Consider two-dimensional motion in an unbounded, inviscid, incompressible and linearly stratified fluid. The linearized Boussinesq equations of motion governing the velocities v, w, the stream function ψ, and ρ', the deviation of the density from its ambient state ρ_0 in which the fluid is at rest, are

$$v = \frac{\partial \psi}{\partial z}, \quad w = -\frac{\partial \psi}{\partial y}, \tag{2.1}$$

$$\frac{\partial \rho'}{\partial t} - \frac{\partial \psi}{\partial y}\frac{\mathrm{d}\rho_0}{\mathrm{d}z} = 0, \tag{2.2}$$

$$\frac{\partial^2}{\partial t^2}\nabla^2\psi + N^2\frac{\partial^2 \psi}{\partial y^2} = 0, \tag{2.3}$$

where a coordinate system is chosen such that the z-axis points upwards and the y-axis points in the horizontal direction to the right. $N = (-(g/\rho_0)(\mathrm{d}\rho_0/\mathrm{d}z))^{\frac{1}{2}}$ is the Brunt–Väisälä frequency, henceforth abbreviated to B.V. frequency, and g is the gravitational acceleration along the negative z-axis. Note that in addition to ψ, ρ' as well as the vorticity $\Omega = -\nabla^2\psi$ also satisfy equation (2.3).

The exact solution of equation (2.3) for the initial conditions corresponding to a partially mixed, cylindrical wake has been obtained by Hartman & Lewis (1972) using Fourier analysis. Their results can be generalized; letting f be either ρ', ψ or Ω, the solution of equation (2.3) for the arbitrary initial conditions $f(y, z, 0)$ and $(\partial f/\partial t)|_{t=0}$ is,

$$f(y,z,t) = \frac{1}{4\pi^2}\int_{-\infty}^{\infty}\int_{-\infty}^{\infty}\frac{1}{2}\left[F_1(k_y,k_z) \pm \frac{F_2(k_y,k_z)}{\mathrm{i}\omega}\right]\mathrm{e}^{\mathrm{i}(k_y y + k_z z \pm \omega t)}\,\mathrm{d}k_y\,\mathrm{d}k_z, \tag{2.4}$$

in which

$$\omega = Nk_y(k_y^2+k_z^2)^{-\frac{1}{2}}, \tag{2.5}$$

$$F_1(k_y,k_z) = \int_{-\infty}^{\infty}\int_{-\infty}^{\infty} f(y,z,0)\,\mathrm{e}^{-\mathrm{i}(k_y y+k_z z)}\,\mathrm{d}y\,\mathrm{d}z, \tag{2.6}$$

$$F_2(k_y,k_z) = \int_{-\infty}^{\infty}\int_{-\infty}^{\infty} \left.\frac{\partial f}{\partial t}\right|_{t=0} \mathrm{e}^{-\mathrm{i}(k_y y+k_z z)}\,\mathrm{d}y\,\mathrm{d}z, \tag{2.7}$$

and the results of the integrals in (2.4) for each sign should be superposed.

In the following, (2.4) will be evaluated for three different sets of initial conditions: a smoothed version of the density perturbation used by Hartman & Lewis, hereinafter referred to as HL, a velocity perturbation simulating the swirl flow, and the velocity perturbation due to a single vortex. The far-field and long-time asymptotic forms of these solutions will also be given. The results of a numerical evaluation of (2.4) for each case will be presented in the form of density contour plots. Finally, all of these linear calculations will be compared with the results of a finite-difference computer code, which solves the fully nonlinear Navier–Stokes equations in the Boussinesq approximation, for the same initial conditions.

2.2. *Finite-difference method*

Using rectangular Cartesian coordinates (x,y,z), we define x as the axial mean flow direction, y and z as the horizontal and vertical directions, respectively, and (v,w) as the corresponding components of the fluid velocity. The equilibrium density ρ_0 is assumed to be a function of the vertical coordinate z only. Neglecting streamwise diffusion and applying the Boussinesq approximation, we obtain the following equations of motion for an inviscid and incompressible fluid:

$$\frac{\partial v}{\partial t} = -\frac{1}{\rho_0}\frac{\partial p}{\partial y} - \frac{\partial v^2}{\partial y} - \frac{\partial vw}{\partial z}, \tag{2.8}$$

$$\frac{\partial w}{\partial t} = -\frac{1}{\rho_0}\frac{\partial p}{\partial z} - \frac{\partial vw}{\partial y} - \frac{\partial w^2}{\partial z} - \frac{\rho' g}{\rho_0}, \tag{2.9}$$

$$\frac{\partial \rho'}{\partial t} = -\frac{\partial v\rho'}{\partial y} - \frac{\partial w\rho'}{\partial y} - w\frac{\mathrm{d}\rho_0}{\mathrm{d}z}, \tag{2.10}$$

$$\frac{\partial v}{\partial y} + \frac{\partial w}{\partial z} = 0, \tag{2.11}$$

where t is time and p is the pressure, (2.8)–(2.11) are a system of equations suitable for calculation of two-dimensional unsteady flows. Given a consistent set of information on an initial (y,z)-plane, equations (2.8)–(2.10) can be used to 'march' in time to obtain the evolving flow field.

The finite-difference formulation of the above equations is similar to the scheme used by Chan (1977), except for a difference in the order of numerical accuracy. Chan used an explicit two-level time-integration scheme with a second-order Taylor series expansion in the marching direction, while in this paper we have retained a third-order accuracy in the marching direction. Centred differencing is used in all space derivatives. Marching of any variable ϕ is obtained via a Taylor series expansion in time, i.e.

$$\phi^{n+1} = \phi^n + \left(\frac{\partial\phi}{\partial t}\right)^n \Delta t + \left(\frac{\partial^2\phi}{\partial t^2}\right)^n \tfrac{1}{2}\Delta t^2 + \left(\frac{\partial^3\phi}{\partial t^3}\right)^n \tfrac{1}{6}\Delta t^3 + O(\Delta t^4).$$

The superscripts $n+1$ and n denote the time levels. The first-order derivatives $(\partial\phi/\partial t)$ are obtained directly from (2.8)–(2.10). For the second- and third-order derivatives, the right-hand side of equations (2.8)–(2.10) are differentiated with respect to t and a conservative flux-form differencing is applied.

The corresponding pressure field is obtained by a modified MAC method by Harlow & Welch (1965). Let $\tilde{v}$ and $\tilde{w}$ denote all the terms in the Taylor series expansion for v and w excluding the pressure terms, so that we have

$$v^{n+1} = \tilde{v}^n - \frac{\partial p}{\partial y}\bigg|^{n+1} \Delta t - \frac{\partial^2 p}{\partial t\,\partial y}\bigg|^{n} \tfrac{1}{2}\Delta t^2,$$

$$w^{n+1} = \tilde{w}^n - \frac{\partial p}{\partial z}\bigg|^{n+1} \Delta t - \frac{\partial^2 p}{\partial t\,\partial z}\bigg|^{n} \tfrac{1}{2}\Delta t^2.$$

Substituting these expressions into the incompressibility condition, equation (2.11), we obtain a Poisson equation for pressure

$$\frac{\partial}{\partial y}\left(\frac{\partial p}{\partial y}\right)^{n+1} + \frac{\partial}{\partial z}\left(\frac{\partial p}{\partial z}\right)^{n+1} = \frac{4}{5\Delta t}\left(\frac{\partial \tilde{v}}{\partial y} + \frac{\partial \tilde{w}}{\partial z}\right)^{n} + \frac{1}{5}\left[\frac{\partial}{\partial y}\left(\frac{\partial p}{\partial y}\right)^{n-1} + \frac{\partial}{\partial z}\left(\frac{\partial p}{\partial z}\right)^{n-1}\right]. \tag{2.12}$$

Equation (2.12) is solved using the method of successive overrelaxation (SOR).

The above numerical scheme is stable and accurate to $(\Delta t)^2$ so long as the marching increment satisfies the Courant–Friedrichs–Lewy condition. The entire system of equations is formulated on a staggered variable mesh. The mesh stretching is carefully designed to prevent unrealistic wave reflections for a linearly stratified fluid. Details of this variable mesh are described in Appendix A of Han, Meng & Innis (1983) where results of using an open boundary condition are also described.

3. Smoothed density perturbation

3.1. *Analytical solution*

HL considered the problem stated in §2 for the initial conditions

$$\rho' = \begin{cases} \epsilon z & (r \leqslant a), \\ 0 & (r > a), \end{cases} \tag{3.1}$$

$$\frac{\partial \rho'}{\partial t} = 0, \tag{3.2}$$

where r is the radial coordinate, $r = (y^2+z^2)^{\frac{1}{2}}$, and ϵ is a density gradient. The discontinuity in the initial value of ρ' at $r = a$ results in a solution possessing an unphysical behaviour there.

To remove that discontinuity, we replace the initial condition (3.1) with a more realistic profile

$$\rho' = \epsilon r \sin(\theta+\alpha)\, \mathrm{e}^{-(r/r_0)^2} \tag{3.3}$$

where θ is the polar angle measured from the horizontal, α is a tilt angle measured from the vertical and r_0 is a characteristic length related to the radius of the wake. This density distribution is a generalization of (3.1), and it is continuous everywhere. It corresponds to a smoothed version of (3.1), with the exception of the added tilt angle α.

For the perturbed density field, the exact solution of (2.3) with the initial conditions (3.2) and (3.3) is found to be

$$\frac{\rho'(x,t)}{\rho_0} = \frac{\epsilon r_0^4}{8\rho_0}\left\{z\cos\alpha\int_0^\infty k^3\,\mathrm{e}^{-\frac{1}{4}(kr_0)^2}\left[\frac{J_1(L^+)}{L^+}+\frac{J_1(L^-)}{L^-}\right]\mathrm{d}k\right.$$
$$\left.+\sin\alpha\int_0^\infty k^2\,\mathrm{e}^{-\frac{1}{4}(kr_0)^2}\left[(ky+Nt)\frac{J_1(L^+)}{L^+}-(ky-Nt)\frac{J_1(L^-)}{L^-}\right]\mathrm{d}k\right\}, \quad (3.4)$$

where $$L^\pm = ((ky\pm Nt)^2+(kz)^2)^{\frac{1}{2}}, \quad k=(k_y^2+k_z^2)^{\frac{1}{2}},$$

and J_1 is the first-order Bessel function of the first kind.

Expression (3.4) is evaluated by first observing that

$$\frac{J_1(L^+)}{L^+}+\frac{J_1(L^-)}{L^-} = \frac{4}{Ntkr}\sum_{l=0}^{\infty}(2l+1)J_{2l+1}(Nt)J_{2l+1}(kr)\frac{\sin[(2l+1)\theta]}{\sin\theta}, \quad (3.5)$$

and

$$\frac{J_1(L^+)}{L^+}-\frac{J_1(L^-)}{L^-} = -\frac{4}{Ntkr}\sum_{l=1}^{\infty}2lJ_{2l}(Nt)J_{2l}(kr)\frac{\sin(2l\theta)}{\sin\theta}, \quad (3.6)$$

[see 9.1.80 in Abramowitz & Stegun (1972) and HL; hereinafter, Abramowitz & Stegun (1972) will be referred to as HMF].

Substituting (3.5) and (3.6) into (3.4) and evaluating the resulting integrals according to 11.4.28 in HMF, we obtain the following result,

$$\frac{\rho'(r,\theta,t)}{\rho_0} = \frac{\epsilon}{\rho_0}\frac{r_0^2}{r}\left\{-\sin\alpha\sum_{l=1}^{\infty}2l\frac{\Gamma(l+1)}{\Gamma(2l+1)}\left(\frac{r}{r_0}\right)^{2l}\frac{\sin(2l\theta)}{\sin\theta}\right.$$
$$\times J_{2l}(Nt)\,M\left[l+1,2l+1,-\left(\frac{r}{r_0}\right)^2\right]$$
$$+\frac{2}{Nt}\frac{r}{r_0}\sin(\theta+\alpha)\sum_{l=0}^{\infty}(2l+1)\frac{\Gamma(l+2)}{\Gamma(2l+2)}\left(\frac{r}{r_0}\right)^{2l+1}\frac{\sin[(2l+1)\theta]}{\sin\theta}$$
$$\left.\times J_{2l+1}(Nt)\,M\left[l+2,2l+2,-\left(\frac{r}{r_0}\right)^2\right]\right\}, \quad (3.7)$$

where M represents the confluent hypergeometric function.

Similarly, the stream function is,

$$\psi = -\tfrac{1}{2}\epsilon N r_0^2\left(\frac{\mathrm{d}\rho_0}{\mathrm{d}z}\right)^{-1}\left\{2\sin(\theta+\alpha)\sum_{l=1}^{\infty}(2l)\frac{\Gamma(l+1)}{\Gamma(2l+1)}\left(\frac{r}{r_0}\right)^{2l}\frac{\sin(2l\theta)}{\sin\theta}\right.$$
$$\times\frac{J_{2l}(Nt)}{Nt}M\left[l+1,2l+1,-\left(\frac{r}{r_0}\right)^2\right]$$
$$-\sin\alpha\sum_{l=0}^{\infty}(2l+1)\frac{\Gamma(l+2)}{\Gamma(2l+2)}\left(\frac{r}{r_0}\right)^{2l}\frac{\sin[(2l+1)\theta]}{\sin\theta}$$
$$\left.\times J_{2l+1}(Nt)\,M\left[l+1,2l+2,-\left(\frac{r}{r_0}\right)^2\right]\right\}, \quad (3.8)$$

and the vorticity is

$$\Omega = 2\epsilon N\left(\frac{\mathrm{d}\rho_0}{\mathrm{d}z}\right)^{-1}\left\{2\sin(\theta+\alpha)\sum_{l=1}^{\infty}(2l)\frac{\Gamma(l+2)}{\Gamma(2l+1)}\left(\frac{r}{r_0}\right)^{2l}\frac{\sin(2l\theta)}{\sin\theta}\right.$$
$$\times\ \frac{J_{2l}(Nt)}{Nt}M\left[l+2,2l+1,-\left(\frac{r}{r_0}\right)^2\right]$$
$$-\sin\alpha\sum_{l=0}^{\infty}(2l+1)\frac{\Gamma(l+2)}{\Gamma(2l+2)}\left(\frac{r}{r_0}\right)^{2l}\frac{\sin[(2l+1)\theta]}{\sin\theta}$$
$$\left.\times J_{2l+1}(Nt)M\left[l+2,2l+2,-\left(\frac{r}{r_0}\right)^2\right]\right\}. \tag{3.9}$$

All these solutions are continuous functions for all r and θ.

For $r/r_0 \to \infty$, the asymptotic expression for the confluent hypergeometric function (see 13.1.5 in HMF) can be used to obtain the following far-field expressions,

$$\left.\frac{\rho'}{\rho_0}\right|_{r/r_0\to\infty} = \epsilon\frac{r_0}{\rho_0}\left(\frac{r}{r_0}\right)^{-3}\left\{-\sin\alpha\sum_{l=1}^{\infty}2l^2\frac{\sin(2l\theta)}{\sin\theta}J_{2l}(Nt)\right.$$
$$\left.+\frac{2}{Nt}\sin(\theta+\alpha)\sum_{l=0}^{\infty}(2l+1)(l+1)\,l\frac{\sin(2l+1)\theta}{\sin\theta}J_{2l+1}(Nt)\right\}. \tag{3.10}$$

For $Nt \to \infty$, the Bessel functions in (3.7)–(3.9) can be reduced using 9.2.1 in HMF and the result shows the long-time asymptotic forms of ρ' for $\alpha = 0$ decay as $(Nt)^{-\frac{3}{2}}$.

The far-field solutions can also be derived directly from (3.4) using the method of stationary phase (Erdelyi 1953). Using this method and specifically for internal waves in a linearly stratified fluid, Lighthill (1978) derived useful formulae and provided physical insight into the results. We used Lighthill's approach, a variant of the relationship 9.1.21 in HMF to represent $J_1(L^{\pm})/L^{+}$, and twice applied the method of stationary phase to the resulting integral and obtained the following result for $\alpha = 0$ case,

$$\frac{\rho'}{\rho_0} \sim \frac{\epsilon z r_0^2}{8r^2}\cot\theta\left(\frac{Ntr_0\cos\theta}{r}\right)^2 \mathrm{e}^{-\frac{1}{4}(Ntr_0\cos\theta/r)^2}\sin(Nt\sin\theta). \tag{3.11}$$

Substituting (3.18) below into the above equation in terms of the parameter a in HL's notation, we have

$$\frac{\rho'}{\rho_0} \sim \frac{\epsilon z a^2}{r^2}\cot\theta\frac{1}{4}\left(\frac{Ntr_0\cos\theta}{r}\right)^2 \mathrm{e}^{-\frac{1}{4}(Ntr_0\cos\theta/r)^2}\sin(Nt\sin\theta). \tag{3.12}$$

Comparing (3.12) with (26) in HL, we find that by changing (3.1) into (3.3), the factor $2J_2(Ntr_0\cos\theta/r)$ which represents variable phase due to the discontinuity at $r = a$ (see Lighthill 1978, p. 435) is replaced by a positive non-oscillatory factor $\frac{1}{4}(Ntr_0\cos\theta/r)^2\,\mathrm{e}^{-\frac{1}{4}(Ntr_0\cos\theta/r)^2}$.

Since (3.11) applies only along a ray, i.e. $Nt\sin\theta = kr$, it can be reduced to,

$$\left.\frac{\rho'}{\rho_0}\right|_{\mathrm{ray}} \sim \frac{\epsilon z r_0^2}{8r^2}\cot\theta(kr_0\cot\theta)^2\,\mathrm{e}^{-\frac{1}{4}(kr_0\cot\theta)^2}\sin(kr), \tag{3.13}$$

which has a maximum, i.e. the most energetic ray, at

$$\tan\theta = \frac{kr_0}{\sqrt{6}}, \tag{3.14}$$

or $\theta = 52°$ with wavelength $= 2r_0$, and the rays will be progressively horizontal as the wavelength increases. This result is consistent with Wu's observation of the rays.

3.2. *Discussion of the analytical result*

It is interesting to compare (3.10) with HL's asymptotic result [equation (25) in their paper], which is reproduced here, using our notation for convenience

$$\left.\frac{\rho'}{\rho_0}\right|_{r/a\to\infty} = \frac{2\epsilon z a^2}{\rho_0 r^2}\sum_{l=1}^{\infty}(2l+1)\frac{\sin[(2l+1)\theta]}{\sin\theta}\frac{J_{2l+1}(Nt)}{Nt}\left[\tfrac{1}{2}l^2\left(\frac{a}{r}\right)^2\right]. \tag{3.15}$$

Note that $J_2(2la/r)$ has been replaced by its limiting value $\frac{1}{2}l^2(a/r)^2$, for $2la/r \to 0$ (see 9.1.7 in HMF). For the case of interest, $\alpha = 0$, and equation (3.10) can be manipulated into the form

$$\left.\frac{\rho'}{\rho_0}\right|_{r/a\to\infty} = \frac{2\epsilon z a^2}{\rho_0 r^2}\sum_{l=1}^{\infty}(2l+1)\frac{\sin[(2l+1)\theta]}{\sin\theta}\frac{J_{2l+1}(Nt)}{Nt}\left[l(l+1)\left(\frac{r_0}{a}\right)^4\left(\frac{a}{r}\right)^2\right]. \tag{3.16}$$

A relationship between the two parameters a and r_0 is needed at this point. A reasonable criterion which will provide this relationship is to require the total potential energy contained in the initial density distribution be the same in both cases. Thus, using the following formula for the potential energy in a stratified fluid,

$$\text{P.E.} = \frac{g}{-2\,\mathrm{d}\rho_0/\mathrm{d}z}\int_0^{\infty}\int_0^{2\pi}\rho'^2 r\,\mathrm{d}\theta\,\mathrm{d}r, \tag{3.17}$$

the initial total potential energies for HL's initial conditions, i.e. from (3.1) and (3.2) and for the present initial conditions, i.e. from (3.2) and (3.3), are calculated.

Equating the results gives the desired relationship between a and r_0,

$$\left(\frac{r_0}{a}\right)^4 = 2. \tag{3.18}$$

Substitute (3.18) into (3.16), and take into consideration the fact that the approximation made by HL is valid only for $r^2/a^2 \gg l \gg 1$; therefore $l(l+1) \approx l^2$ in (3.16), we can see that the smoothed initial distribution produces a far-field effect which is of the same form as that of the discontinuous initial distribution, but it is four times larger even though the initial total potential energy is the same in both cases. The conclusion can therefore be drawn that, in the discontinuous case, a portion of the total energy is 'trapped' at $r = a$ where the fluid oscillates persistently, as described by HL, and does not radiate to the far field; while in our smoothed case no energy is trapped. The amount of energy trapped in the HL's discontinuous case accounts for the smaller far-field amplitude.

3.3. *Discussion of the density contours*

In order to gain some physical insight into the internal wave field generated by the collapse of a well-mixed region, (3.7) has been evaluated up to $Nt = 10$ cycles for the fully mixed case with no wake tilt, that is, the $\epsilon = -\mathrm{d}\rho_0/\mathrm{d}z$ and $\alpha = 0$ case. The

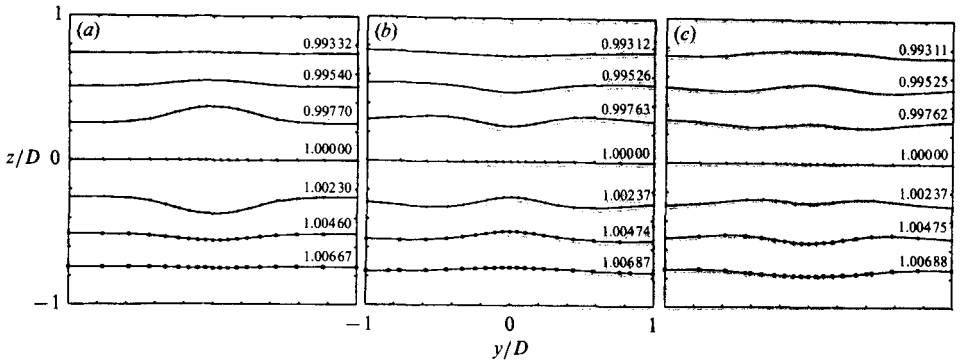

FIGURE 1. Linear internal waves generated by a smoothed density perturbation in an inviscid and linearly stratified fluid. $g/N^2D = 110.48$, $r_0/D = 0.346$, $(Nt/2\pi)$: (*a*) 0 cycle, (*b*) 0.59 cycle, (*c*) 1.18 cycle.

infinite series is evaluated term by term until the individual term contributes less than 10^{-6} of the computed partial sum. The series converges rapidly, requiring the evaluation of the first six to eleven terms. It converges more slowly as Nt or r/D increase. Contours of the density $\rho = \rho_0(z) + \rho'$ are given in the figure 1 series at three different times, $Nt = 0$, 0.59 and 1.18 cycles. The density is normalized to be unity at $z = 0$. The ticks and dots indicate the location of the mesh points where the infinite series is evaluated. This variable mesh is identical to the one used in the finite-difference solution to be discussed in §3.4.

The input conditions are $r_0/D = 0.346$ and $N = 0.094$ rad/s. These are chosen to allow later intercomparison with the velocity disturbance cases. The length D is an arbitrary but common lengthscale also chosen for later comparisons of all density contour plots. A non-dimensional parameter, $\tilde{g} = g/N^2D = 110.91$ similar to a Froude number is obtained, which says the water density is much greater than the density disturbance, a necessary linear condition. The coefficient in (3.7) can be expressed as

$$\frac{\epsilon r_0}{\rho_0} = \frac{r_0}{D}\frac{1}{\tilde{g}} = 3.12 \times 10^{-3},$$

for the case to be reported here.

Note that in figure 1 (*a*), the density field is symmetric with respect to the z-axis and antisymmetric with respect to the y-axis. This property holds true at all times and is self-evident from (3.7) where $\alpha = 0$. The maximum initial vertical displacement can be computed from (3.3) as

$$\left.\frac{\zeta}{D}\right|_{\text{maximum}} = -\frac{\rho'}{\mathrm{d}\rho_0/\mathrm{d}z}\frac{1}{D} = \frac{1}{(2e)^{\frac{1}{2}}}\frac{r_0}{D} \cong 0.15,$$

at $z/D = \pm(1/\sqrt{2})(r_0/D) \cong \pm 0.24$, which is close to the apparent displacement of the third and fifth contours, counting from the top.

Figure 1 (*b*) shows a symmetric internal wave pattern at approximately half of a B.V. period after the initial disturbance is released. The phase of the internal wave, as expected, is completely reversed; the centre portion is going through a 'collapse' motion. Connecting the wave crests or troughs one can see that an angle of 43° is evident in figure 1 (*b*) and 50° in figure 1 (*c*). This ray angle was observed by Wu (1969) in his experimental study of a turbulent mixed region, where he found that angle is $= 3\pi/10$ or 54° from the horizontal direction, and is also consistent with (3.14).

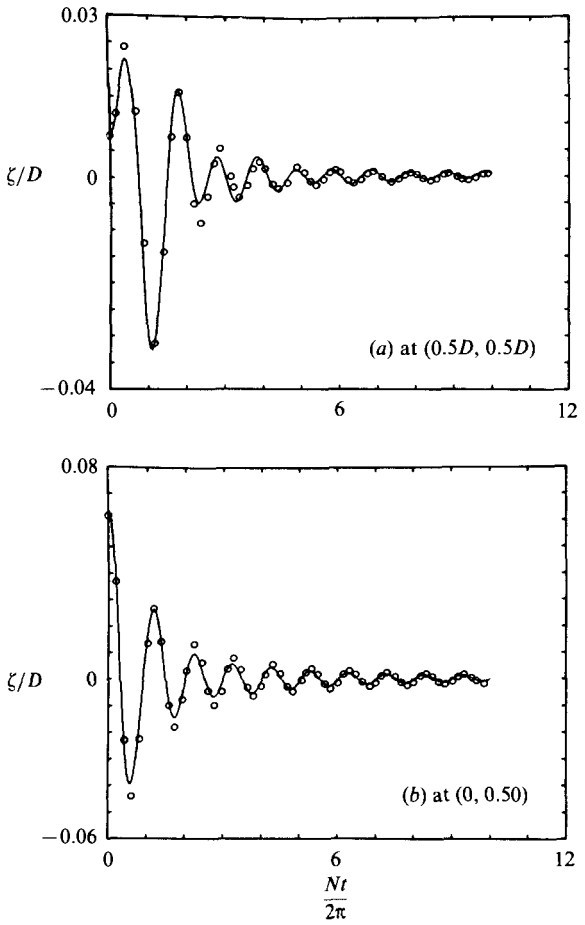

FIGURE 2. The isopycnic displacements vs. B.V. period at two positions on the computational plane for the smoothed density perturbation case. ——, numerical solution of the fully nonlinear Navier–Stokes equation; ○, linear theory.

3.4. *Comparison with finite-difference solution*

The results presented in §3.3 can be compared with the outputs of the finite-difference method which solves the fully nonlinear Navier–Stokes equations.

One difficulty in making the comparison is that the solution presented in §3.1 is for an unbounded fluid, but a bounded computational domain is required when solving the equations by a computer code, which uses 'free-slip wall' boundary conditions. After some experimentation, it was found that a computational domain of dimensions $40D$ in the horizontal direction and $40D$ in the vertical direction was sufficiently large to make any disturbance in the flow due to the solid boundaries negligible in the region of interest. The alternative is to use an 'open wall' boundary condition, results of which are given by Han, Meng & Innis (1983). In calculations presented here the computational effort is reduced by observing that the symmetry of the flow requires that only one quadrant of the flow field be computed.

The results of the finite-difference method and that from (3.7) are shown in figures 2(*a*) and (*b*) in terms of the time history of the isopycnic displacement at three near-field locations on the computational plane. The agreement is remarkably good. Note

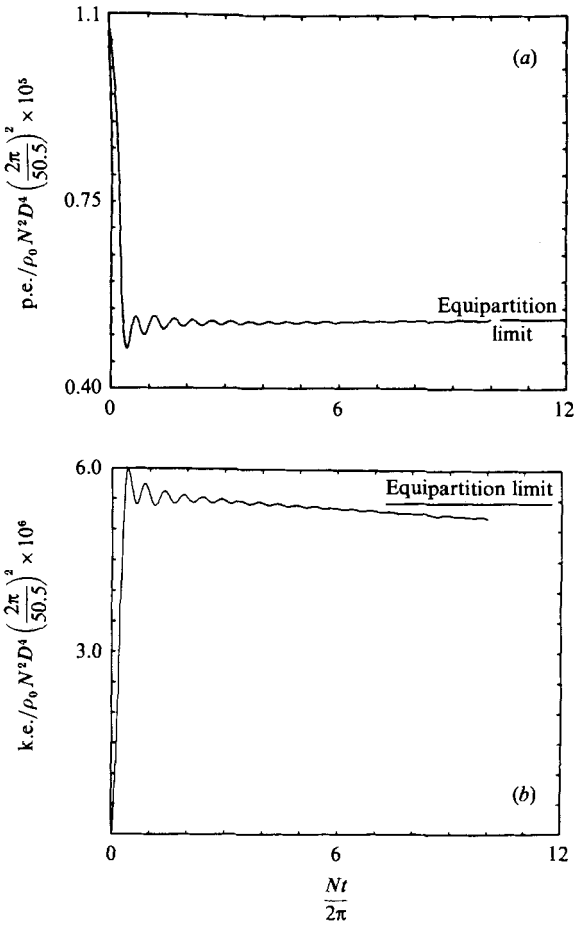

FIGURE 3. Energies per unit length on the computational plane vs. B.V. period for the smoothed density perturbation case. (*a*) Potential energy. (*b*) Kinetic energy.

that, after the initial collapse, the envelopes of the curves have the predicted $(Nt)^{-\frac{3}{2}}$ asymptotic behaviour. This clearly shows that the fully mixed wake-collapse problem falls well within the realm of the linear approximation.

The small discrepancies that do exist between the two methods are believed to be due to the variable mesh applied in the computer code, i.e. the finite-difference mesh becomes coarser as the distance from the wake centre increases. Figure 3 (*a*, *b*) shows the history of the potential and kinetic energies in the computational plane. After the initial collapse, the potential energy is seen to remain, on average, constant, but the kinetic energy shows an average decline; the total energy, therefore, does not remain constant. The total energy loss is approximately 5%. One origin of the kinetic energy loss is that the flow divergence $\nabla \cdot \boldsymbol{u}$ is not exactly zero, so that it only affects the velocity equations, hence the kinetic energy, not the density equation which does not depend upon the pressure gradient. Another origin is the strong stretching of the variable mesh which eliminates the short-wavelength waves as they propagate into the coarse mesh region. However, a rigorous demonstration of this has not been attempted, although some relevant results using an 'open' boundary condition are discussed in Han *et al.* (1983).

Two noteworthy points can be made about figure 3. First, initially the total energy of the flow is all contained in potential energy form, the value of which can easily be calculated from (3.17). Since only a quadrant of the flow is calculated, figure 3 shows only a quarter of the energies. Second, at about half of a B.V. period, the flow reaches an equilibrium state; namely the energy is equi-partitioned into potential and kinetic energies, and the kinetic energy drifts below half of the total energy released initially.

4. Swirl-flow perturbation

4.1. *Analytical formulation*

An analytical representation of a propeller-generated swirl velocity profile is obtained. The details will not be given here, however; the essence is briefly described below. We solve the one-dimensional axisymmetric equations of motion in a non-stratified fluid. By introducing a self-similar variable $\eta = r/(2\nu t)^{\frac{1}{2}}$, where r is the radial coordinate and ν is the kinematic viscosity, we find for the laminar flow case, the circumferential swirl velocity profile:

$$v_\theta = \frac{C_1}{t^{\frac{3}{2}}} \eta \, \mathrm{e}^{-\frac{1}{2}\eta^2},$$

where C_1 is a constant. Similarly, for turbulent case with η being the turbulent eddy viscosity and C_2 another constant, we obtain

$$v_\theta = \frac{C_2}{t^{\frac{3}{4}}} \eta \, \mathrm{e}^{-2\eta^2},$$

or,

$$v_\theta = V_0 \frac{r}{r_0} \mathrm{e}^{-2(r/r_0)^2}, \tag{4.1}$$

with $r_0 = (2\nu t)^{\frac{1}{2}}$. Equation (4.1) is applied here as the initial condition. In addition, we consider the density field to be initially undisturbed,

$$\rho' = 0. \tag{4.2}$$

The remaining initial condition is obtained by substituting the velocity perturbation (4.1) into (2.2),

$$\frac{\partial \rho'}{\partial t} = -V_0 \left(\frac{r}{r_0}\right) \cos\theta \, \mathrm{e}^{-2(r/r_0)^2} \frac{\mathrm{d}\rho_0}{\mathrm{d}z}. \tag{4.3}$$

From (2.4) and the initial conditions (4.2) and (4.3), we obtain the exact result,

$$\frac{\rho'(\boldsymbol{x}, t)}{\rho_0} = -\frac{V_0 r_0^3}{32g} N \int_0^\infty k^2 \, \mathrm{e}^{-\frac{1}{8}(kr_0)^2} [J_0(L^+) - J_0(L^-)] \, \mathrm{d}k, \tag{4.4}$$

where $L^\pm$ is defined in §3. Physically, $J_0(L^\pm)$ represent left and right propagating waves.

Expression (4.4) can be evaluated in a manner similar to that which was used in §3 by substituting the following relation (see 9.1.79 in HMF),

$$J_0(L^+) - J_0(L^-) = -4 \sum_{l=0}^{\infty} J_{2l+1}(Nt) J_{2l+1}(kr) \cos[(2l+1)\theta], \tag{4.5}$$

into (4.4) and evaluating the resulting integrals (see 11.4.28 in HMF) to obtain,

$$\frac{\rho'(r,\theta,t)}{\rho_0} = \frac{2^{\frac{1}{2}}V_0}{g} N \sum_{l=0}^{\infty} \frac{\Gamma(l+2)}{\Gamma(2l+2)} \left(\sqrt{2}\frac{r}{r_0}\right)^{2l+1} \cos[(2l+1)\theta] \times J_{2l+1}(Nt) M\left[l+2, 2l+2, -2\left(\frac{r}{r_0}\right)^2\right]. \quad (4.6)$$

The stream function and vorticity are determined in a similar fashion; they are,

$$\psi = \tfrac{1}{4}V_0 r_0 J_0(Nt)\, e^{-2(r/r_0)^2} + \tfrac{1}{2}V_0 r_0 \sum_{l=1}^{\infty} \frac{\Gamma(l+1)}{\Gamma(2l+1)} \left(\sqrt{2}r\frac{r}{r_0}\right)^{2l} \cos 2l\theta \times J_{2l}(Nt) M\left[l+1, 2l+1, -2\left(\frac{r}{r_0}\right)^2\right], \quad (4.7)$$

and

$$\Omega = 2\frac{V_0}{r_0} J_0(Nt)\left[1-2\left(\frac{r}{r_0}\right)^2\right] e^{-2(r/r_0)^2} + 4\frac{V_0}{r_0} \sum_{l=1}^{\infty} \frac{\Gamma(l+2)}{\Gamma(2l+1)} \left(2^{\frac{1}{2}}\frac{r}{r_0}\right)^{2l} \cos 2l\theta \times J_{2l}(Nt) M\left[l+2, 2l+1, -2\left(\frac{r}{r_0}\right)^2\right]. \quad (4.8)$$

The first terms in (4.7) and (4.8) represent time-dependent local non-propagating disturbance, while the second terms represent the propagating internal waves. Notice that in (3.8) and (3.9) no such local disturbances exist, owing to the absence of the initial velocity perturbation.

Again using the asymptotic expression for the confluent hypergeometric function (13.1.5 in HMF), we can obtain the far-field expressions for (4.6)–(4.8). It can be shown that the internal wave amplitude, the stream function and vorticity produced by a swirl all decay with r in the far field at the same rates as those produced by the smoothed density perturbation. The asymptotic expression as $Nt \to \infty$ for the swirl induced ρ' decays as $(Nt)^{-\frac{1}{2}}$, a rate three times slower than the smoothed density case. The stationary phase result can be shown to be,

$$\left.\frac{\rho'}{\rho_0}\right|_{\text{ray}} \sim -\frac{V_0 N r_0}{32gr}\left(\frac{Ntr_0\cos\theta}{r}\right)^2 e^{-\frac{1}{8}(Ntr_0\cos\theta/r)^2} \cos(Nt\sin\theta), \quad (4.9)$$

which shows a slower decay than (3.11). Along a ray $Nt\sin\theta = kr$, so that (4.9) is reduced to,

$$\left.\frac{\rho'}{\rho_0}\right|_{\text{ray}} \sim -\frac{V_0 N r_0}{32gr}(kr_0\cot\theta)^2\, e^{-\frac{1}{8}(kr_0\cot\theta)^2} \cos(kr), \quad (4.10)$$

which has a maximum at $\tan\theta = kr_0/2\sqrt{2}$, or $\theta = 48°$ at $kr_0 = \pi$. A result very similar to the density-perturbation case.

4.2. *Discussion of the analytical result*

One interesting physical quantity introduced by the swirl motion into a stratified fluid is the angular momentum. Since the gravity does exert a torque on an asymmetric (with respect to the vertical axis) density anomaly field, it is desirable to understand how both the torque and angular momentum vary with time.

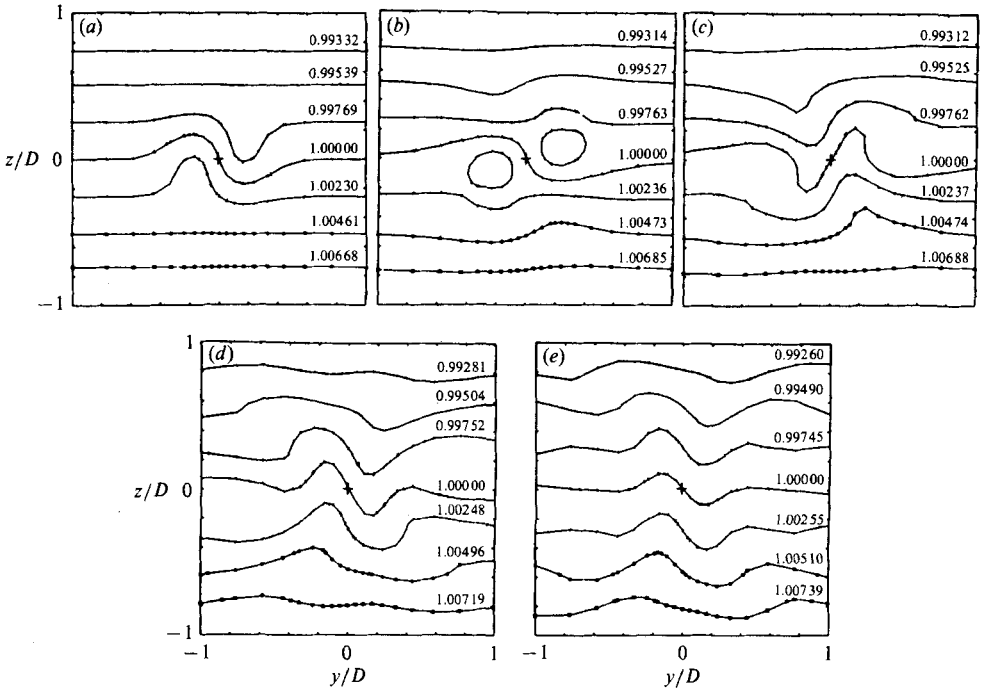

FIGURE 4. Linear internal waves generated by a swirling velocity perturbation in an inviscid and linearly stratified fluid. +, centre of the swirl. $g/N^2D = 110.48$, $2\pi V_0/ND = 8.342$, $r_0/D = 0.346$, $Nt/2\pi$: (*a*) 0.12 cycle, (*b*) 0.48 cycle, (*c*) 0.71 cycle, (*d*) 1.31 cycle, (*e*) 2.26 cycle.

The torque per unit length about the origin is obtained by integrating the torque per unit volume over the entire plane,

$$\boldsymbol{T}(t) = \int_0^\infty \int_0^{2\pi} (\boldsymbol{r} \times \rho \boldsymbol{g})\, r\, \mathrm{d}\theta\, \mathrm{d}r = -\hat{\boldsymbol{\imath}} \int_0^\infty \int_0^{2\pi} \rho' r^2 g \cos\theta\, \mathrm{d}\theta\, \mathrm{d}r, \tag{4.11}$$

in which ρ' is the density anomaly and $\hat{\boldsymbol{\imath}}$ is a unit vector perpendiculr to the (y,z)-plane.

Substituting of (4.6) into (4.11) and noting that the integral over θ is zero for every l except $l = 0$, for which the value of the integral is π. Therefore, only the first term in the series is non-zero, and (4.11) reduces to

$$\boldsymbol{T}(t) = -\hat{\boldsymbol{\imath}} V_0 N \rho_0 r_0^2 \frac{\pi}{\sqrt{2}} J_1(Nt) \int_0^\infty \left(\sqrt{2}\frac{r}{r_0}\right)^3 M\left[2, 2, -2\left(\frac{r}{r_0}\right)^2\right] \mathrm{d}r, \tag{4.12}$$

which can be further simplified via 13.6.12 in HMF to

$$\boldsymbol{T}(t) = -\hat{\boldsymbol{\imath}} V_0 N \rho_0 r_0^3 \tfrac{1}{4}\pi J_1(Nt). \tag{4.13}$$

Since the torque is equal to the time rate of change of the angular momentum, the latter can be determined by integrating (4.13) with respect to time; the resulting constant of integration is determined by the initial value of the angular momentum. It can be shown that the angular momentum is

$$\boldsymbol{L}(t) = \hat{\boldsymbol{\imath}} V_0 \rho_0 r_0^3 \tfrac{1}{4}\pi J_0(Nt). \tag{4.14}$$

Both $\boldsymbol{T}$ and $\boldsymbol{L}$ show an interesting oscillation at a frequency slower than, but asymptotically approaching, the B.V. frequency. They are nearly 90° out of phase from each other. The amplitude decays as $(Nt)^{-\frac{1}{2}}$. This can be called a 'torsional pendulum' in analogy to its counterpart in solid mechanics.

4.3. *Discussion of the density contours*

Equation (4.6) has been numerically evaluated up to $Nt = 10$ cycles; the results are shown in figure 4.

The B.V. frequency $N = 0.094$ rad/s, a half radius of the initial swirl profile $r_0/D = 0.346$, and a swirl velocity $V_0 = 1.25$ m/s are chosen for simulating a laboratory experiment, which yields the following non-dimensional parameters

$$\tilde{g} = \frac{gD}{V_0^2} = 62.921, \quad F_{\text{swirl}} = \frac{2\pi V_0}{ND} = 8.342.$$

The coefficient in (4.6) can then be expressed as

$$\sqrt{2}\frac{V_0 N}{g} = \sqrt{2}\frac{2\pi}{\tilde{g}F_{\text{swirl}}} = 1.693 \times 10^{-2}.$$

At $t = 0$, the initial density contour configuration, which is not shown here, corresponds to an ambient state at rest; all contours are flat and horizontal. At 0.12 B.V. periods (figure 4(*a*)) the density contour simply follows the swirl flow which is rotating in the clockwise direction. The swirl brings heavier fluid from below to the left of the wake centre and lighter fluid from above to the right of the wake centre. The density deviation field is symmetric with respect to the y-axis, and antisymmetric with respect to the z-axis, as is evident from (4.6) when θ is replaced by $-\theta$ or $\pi-\theta$. The maximum internal wave amplitude is approximately

$$\frac{\zeta}{D}\bigg|_{\text{maximum}} = -\rho' \frac{1}{\mathrm{d}\rho_0/\mathrm{d}z}\frac{1}{D} \approx \frac{2\pi}{2e^{\frac{1}{2}}}\frac{V_0}{ND}\frac{Nt}{2\pi} \approx 0.3 \quad \text{at } \frac{y}{D} \approx \frac{1}{2}\frac{r_0}{D} = \pm 0.2,$$

which seems in agreement with the numerical results. Very little internal wave energy is radiated from the centre region; the top and bottom contours essentially remain stationary. Half a B.V. period later, at $Nt = 0.48$ periods, figure 4(*b*) shows that the stratification effect is beginning to emerge on the top and bottom contours, while in the centre region, that is, where $|z/D| < 0.2$, the phase of the internal wave is still dominated by the swirl motion. Notice that the slope of the centre contour, that is, the contour for $\rho/\rho_0(0) \equiv 1$, is at an angle of $-65°$ from the horizontal. At about half a B.V. period from $Nt = 0.12$ periods, that is, at $Nt = 0.71$ periods as shown in figure 4(*c*), the phase of the internal wave is completely reversed. Notice, however, that unlike the wake-collapse problem described in the last section, the internal wave amplitude is not significantly reduced. At about a B.V. period from 0.12 B.V. periods, at $Nt = 1.31$ periods (figure 4*d*), the phase is again reversed. The slope of the contour centre is again at about $-64°$. At this time, however, the wave energy has propagated over a much larger area than the initial dimension of the swirl region. Therefore, some attenuation of the internal wave amplitude is expected to emerge. If one measures the peak to trough vertical distance for the centre density contours and tabulates them as a function of Nt,

$$Nt = 0.12,\ 0.48,\ 0.71,\ 1.31,\ 2.26,$$

$$\frac{z}{D}\bigg|_{\text{maximum}} = 0.34,\ 0.31,\ 0.42,\ 0.36,\ 0.21,$$

one sees that the internal wave amplitude grows initially in the first half B.V. period, so that one can expect that it takes about half a B.V. period for the fluid to react to a velocity-perturbation field. After that, the internal wave amplitude decreases slowly according to $(Nt)^{-\frac{1}{2}}$ as compared to the density-perturbation case which decays as $(Nt)^{-\frac{3}{2}}$. It may be reasonable to generalize this observation by suggesting that in the linear limit a velocity-perturbation field generates an internal wave field more persistent than that generated by the density-perturbation field.

In figure 4(*e*) the density contour plot at $Nt = 2.26$ periods is given. The entire flow domain is oscillating in phase. If one connects the wave crests or troughs one can see the almost vertical rays propagating energy directly upwards or downwards which is in strong contrast to the density-perturbation case.

4.4. *Comparison with finite-difference solution*

This comparison is helpful in establishing the range of swirl velocity perturbations over which the linear approximation is valid. It is clear from the density contour plots of §4.3 that the flow for the values of the parameters given in that section is not a linear one, so V_0 must be reduced in order to make a fair comparison. A factor of five reduction in V_0 was found to be a suitable choice. The linear solution is simply proportional to V_0, so the solution for the new value of V_0 is easily obtained from the results of §4.3; the amplitudes of the density contours are reduced by a factor of five. The relevant non-dimensional parameter, which is a measure of the relative importance of the nonlinearity versus the stratification effect, is then $F_{\text{swirl}} = 1.67$.

The readers are reminded that the solution formulated in §4.1 is for an unbounded fluid. Furthermore, this flow, unlike the smoothed density case, has no symmetry properties that can be exploited to reduce the cost of the computation; so that the entire flow field was computed. A computational domain of dimensions $13.10D$ in the horizontal direction and $8D$ in the vertical direction was found to be satisfactory.

Plots comparing the analytical results of §4.1 and the finite-difference solutions in terms of the history of the isopycnic displacements at two near-field locations on the computational plane are presented in figure 5(*a*, *b*). The wake centre is located at the origin of the coordinate system on the computational plane. The agreement is seen to be very good. Note that after the subsidence of the initial swirl impulse, the envelope of these curves have the predicted $(Nt)^{-\frac{1}{2}}$ asymptotic behaviour.

Figure 6 shows the history of the potential energy per unit length on the computational plane as computed by the finite-difference computer code. After the initial swirl impulse, the potential energy is constant, on average, but shows the wall-reflected wave energy near $Nt = 7$ periods. Two points about the energy history should be made here. First, as expected, all the energy is initially in kinetic energy form, at two-tenths of a B.V. period, half of the kinetic energy (not shown) is converted into potential energy – an interesting reversal to the smoothed-density-perturbation case. Second, the equi-partition of energy is reached shortly after 0.4 B.V. periods, similar to the density case. To be more specific, the equi-partition mentioned here is defined as when the half energy mark is crossed the second time.

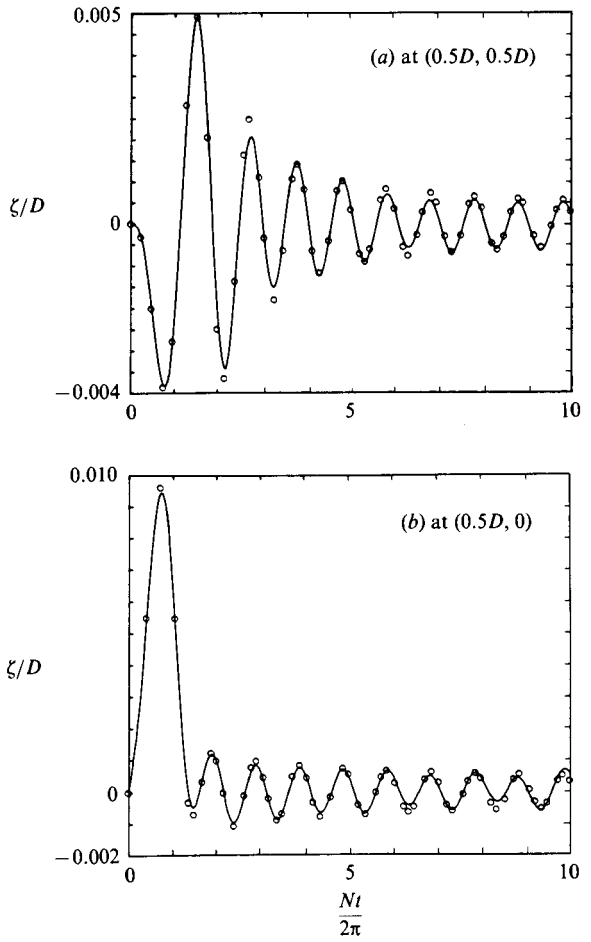

FIGURE 5. The isopycnic displacements vs. B.V. period at two positions on the computational plane for the swirl case. ——, numerical solution of the fully nonlinear Navier–Stokes equations; ○, linear theory.

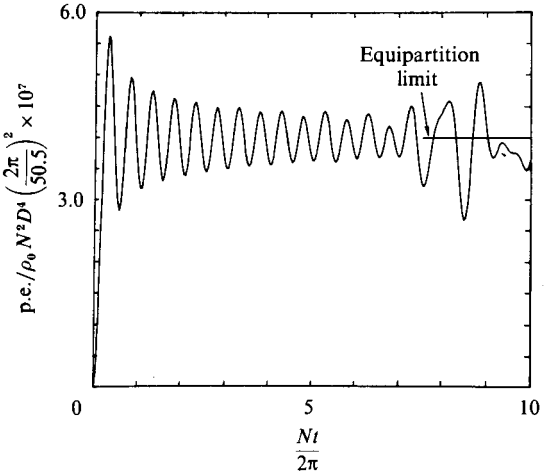

FIGURE 6. The potential energy per unit length on the computational plane vs. B.V. period for the swirl case.

5. Vortex-flow perturbation

5.1. *Analytical solution*

The tangential velocity field v_θ associated with a single vortex with core radius r_0, and located at the origin, can be represented by the following relation, which can be called a modified Rankine-vortex model,

$$v_\theta(r) = \frac{\Gamma_0}{2\pi}\frac{r}{r^2+r_0^2}, \tag{5.1}$$

where Γ_0 is the circulation of the vortex. From (5.1) and (2.2), the initial conditions for the density perturbation corresponding to a single vortex can be determined as

$$\rho' = 0, \tag{5.2}$$

$$\frac{\partial\rho'}{\partial t} = -\frac{\Gamma_0}{2\pi}\frac{\mathrm{d}\rho_0}{\mathrm{d}z}\frac{y}{r^2+r_0^2}. \tag{5.3}$$

Equation (2.4), in this case, can be reduced to the following form

$$\frac{\rho'(r,\theta,t)}{\rho_0} = -\frac{r_0\Gamma_0 N}{4\pi g}\int_0^\infty kK_1(kr_0)[J_0(L^+)-J_0(L^-)]\,\mathrm{d}k, \tag{5.4}$$

in which $L^\pm$ is defined as in §3, and K_1 is the first-order modified Bessel function of the second kind.

Substituting (4.5) into (5.4) and integrating the resulting modified Weber–Schafheitlen integrals (see §13.45 in Watson 1958), we obtain

$$\frac{\rho'(r,\theta,t)}{\rho_0} = \frac{\Gamma_0}{\pi g r_0}N\sum_{l=0}^{\infty}\frac{\Gamma(l+2)\,\Gamma(l+1)}{\Gamma(2l+2)}\left(\frac{r}{r_0}\right)^{2l+1}\cos[(2l+1)\theta] \times J_{2l+1}(Nt)\,F\left[l+1, l+2, 2l+2; -\left(\frac{r}{r_0}\right)^2\right], \tag{5.5}$$

where F represents the hypergeometric function.

In this case, the stream function does not satisfy the boundary condition $\psi\to 0$ as $r/r_0\to\infty$, so due care must be taken in applying the Fourier transform method. However, the result is,

$$\psi = -\frac{\Gamma_0}{4\pi}\left\{\ln(r^2+r_0^2)J_0(Nt) - \sum_{l=1}^{\infty}\frac{\Gamma(l+1)\,\Gamma(l)}{\Gamma(2l+1)}\left(\frac{r}{r_0}\right)^{2l}\cos(2l\theta) \times J_{2l}(Nt)\,F\left[l+1, l; 2l+1; -\left(\frac{r}{r_0}\right)^2\right]\right\}. \tag{5.6}$$

The vorticity field is found to be

$$\Omega = \frac{\Gamma_0}{\pi r_0^2}\left\{\left(1+\frac{r^2}{r_0^2}\right)^{-2}J_0(Nt) + 2\sum_{l=1}^{\infty}\frac{\Gamma(l+2)\,\Lambda(l+1)}{\Gamma(2l+1)}\left(\frac{r}{r_0}\right)^{2l}\cos(2l\theta) \times J_{2l}(Nt)\,F\left[l+2, l+1; 2l+1; -\left(\frac{r}{r_0}\right)^2\right]\right\}. \tag{5.7}$$

As is true in the swirl case, the first terms in (5.6) and (5.7) represent the non-propagating local disturbance at the source.

An asymptotic expression, as $(r/r_0)\to\infty$, for (5.5) can be obtained by first writing

the analytic continuation of the hypergeometric function in the form of an infinite series, as is given on p. 63 of Erdelyi (1953). Then, retaining only the lowest-order term in (r_0/r) the following asymptotic expression for (5.5) can be obtained,

$$\left.\frac{\rho'}{\rho_0}\right|_{r/r_0\to\infty} = \frac{\Gamma_0}{\pi g r_0} N \left(\frac{r}{r_0}\right)^{-1} \sum_{l=0}^{\infty} J_{2l+1}(Nt)\cos[(2l+1)\theta]. \tag{5.8}$$

In a similar manner, the following far-field expression for the vorticity is obtained, while the stream function is, of course, unbounded at infinity.

$$\Omega|_{r/r_0\to\infty} = 2\frac{\Gamma_0}{\pi r_0^2}\left(\frac{r}{r_0}\right)^{-2} \sum_{l=1}^{\infty} l\cos(2l\theta) J_{2l}(Nt). \tag{5.9}$$

It is important to note that the density anomaly and the vorticity decay much more slowly, as $r/r_0 \to \infty$, in the vortex case as opposed to either the smoothed-density-perturbation case or the swirl case.

For $Nt \to \infty$, the asymptotic forms of (5.5)–(5.7) can be obtained by the use of equations (9.2.1) in HMF. We find that ρ' generated by a vortex decays as $(Nt)^{-\frac{1}{2}}$, similar to the swirl case and is a factor of three slower than the density case.

5.2. *A vortex pair in a stratified fluid*

It is a well-known fact that the total kinetic energy associated with a single vortex is infinite, so it does not correspond to any physical process. However, it can be shown (Milne-Thomson 1968), that the velocity field associated with a pair of vortices of equal, but opposite, strength has finite total kinetic energy. Therefore, an extension of the present analysis to the case of a vortex pair is necessary.

In the framework of the linear analysis, the solution of a vortex pair can be obtained by superposing solutions of the single-vortex case. The solution obtained in the previous section was for a single vortex located at the origin, however, so that the solution for a single vortex at an arbitrary position on the plane needs to be obtained by a simple translation of the coordinate system. The solution for a pair is then just the sum of two solutions of this type. Although the solution is simple to obtain, its form is complicated, and this makes it difficult to express in analytic form.

5.3. *Discussion of the numerical result*

Equation (5.5) is evaluated term by term, and the results are shown in figure 7. The hypergeometric function converges at a rate about three times slower than the confluent hypergeometric function, so that the present calculation is more time-consuming than the previous two cases. The solution for a vortex pair, with vortices of circulation strength $\pm\Gamma_0$ located at $y/D = \pm 0.3$, $z/D = 0$, is obtained by superposing two evaluations of (5.5). The initial position of each vortex is marked by a '+'. The calculation was carried out up to $Nt = 5$ cycles. The input conditions are: $r_0 = 0.1D$, the vortex core radius, $b = 0.6D$, the separation distance of the vortices, $N = 0.094$ rad/s same as the previous cases. They are chosen to simulate a laboratory experiment, and we have the following non-dimensional parameters:

$$F_{\text{vorticity}} = \frac{\Gamma_0}{N r_0^2} = 50, \quad F_{\text{vortex}} = \frac{\Gamma_0}{\pi N b^2} = 0.442, \quad \tilde{g} = \frac{g r_0^3}{\Gamma_0^2} = 0.444.$$

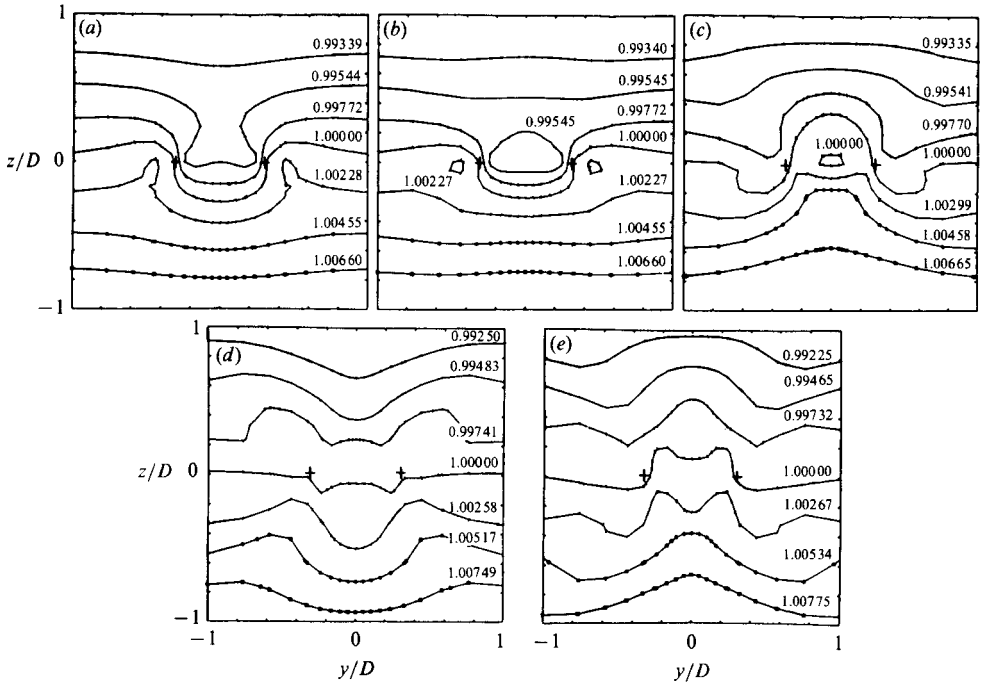

FIGURE 7. Linear internal waves generated by a vortex pair in an inviscid and linearly stratified fluid. +, centres of the vortices. $g/N^2D = 110.48$, $\Gamma/\pi Nb^2 = 0.45$, $r_0/D = 0.1$, $b/D = 0.6$, $Nt/2\pi$: (*a*) 0.2 cycle, (*b*) 0.4 cycle, (*c*) 0.79 cycle, (*d*) 1.19 cycle, (*e*) 1.78 cycle.

The coefficient in (5.5) can then be expressed as

$$\frac{\Gamma_0 N}{\pi g r_0} = \frac{1}{\pi}\frac{1}{\tilde{g}}\frac{1}{F_{\text{vorticity}}} = 0.014.$$

At $t = 0$, the density contour is the ambient stratification profile with all contours flat and horizontal (not shown). The ticks and dots on the contour lines indicate the same variable mesh points to be used in the finite difference calculation in §5.5. At $Nt = 0.2$ cycles shown in figure 7(*a*), the maximum vertical displacement is approximately 0.4. It can also be estimated from the leading term of (5.5) to be

$$\frac{\Gamma_0}{\pi N b^2}\left(\frac{b}{r_0}\right)^2 \frac{b}{D}\frac{\frac{1}{2}Nt}{1+(b/2r_0)^2} \approx 0.6.$$

on the centre line. At this time the fluid is completely dominated by the symmetric vortex-pair motion, the vortex pair acting as if it were in a homogeneous fluid. Very little internal wave energy is radiated away from the region of initial disturbance. At 0.2 B.V. periods later (figure 7*b*), the stratification effect begins to emerge on the top and bottom contours where the phase has reversed, but the centre portion is still dominated by the vortex-pair motion. A portion of the fluid, that is, the closed contour in the centre region with $\rho = 0.99545$, which was originally located at the $z/D \approx 0.5$ level, seems to be trapped by the vortex motion and is kept separated from its original level. Similarly, two smaller blobs of fluid with $\rho = 1.00227$ are separated from their original level at $z/D \approx -0.2$. At about 0.4 B.V. periods later at $Nt = 0.8$ as shown in figure 7(*c*), the phase of the internal wave is completely reversed. The

configuration of the density contour is nearly an upside-down version of figure 7(*a*). Another 0.4 and one B.V. periods later, at $Nt = 1.19$ cycles and $Nt = 1.78$ cycles as shown in figure 7(*d*, *e*), the phase is again reversed and the entire fluid column engages in an oscillation completely in phase. If one connects the crests and troughs, one finds the almost vertical rays along which internal waves propagate energy directly upwards or downwards. This confirms the earlier observation that a vortex perturbation in a stratified fluid introduces a near field depending upon its initial vorticity and decays slowly in proportion to $J_0(Nt)$.

One can tabulate the maximum vertical displacement on the centre line ($y/D = 0$) as a function of Nt,

$$Nt = 0.2,\ 0.4,\ 0.79,\ 1.19,\ 1.78,$$

$$\left.\frac{\zeta}{D}\right|_{\max} = 0.51,\ 0.43,\ 0.34,\ 0.25,\ 0.20,$$

which follows the predicted asymptotic decay law $(Nt)^{-\frac{1}{2}}$ for (5.5) quite closely.

5.4. *Lamb's vortex model*

The analysis of §5.1 is greatly simplified if the velocity field due to a vortex is modelled by the following relation instead of (5.1).

$$V_\theta(r) = \frac{\Gamma_0}{2\pi r}[1 - e^{-(r/r_0)^2}]. \tag{5.10}$$

To elucidate the similarity of (5.10) to (5.1), we observe that (5.10) has the following limiting forms,

$$V_\theta(r) \sim \frac{\Gamma_0}{2\pi r_0}\left(\frac{r}{r_0}\right) \text{ for } \frac{r}{r_0} \to 0, \quad \text{and } \sim \frac{\Gamma_0}{2\pi r} \text{ for } \frac{r}{r_0} \to \infty, \tag{5.11}$$

which matches the behaviour of (5.1) in the same limits. One should also notice that at $r/r_0 = 1$, from (5.10), we have

$$V_\theta(1) = (0.63)\frac{\Gamma}{2\pi r_0}, \tag{5.12}$$

which is comparable to that obtained from (5.1)

$$V_\theta(1) = (0.5)\frac{\Gamma_0}{2\pi r_0}. \tag{5.13}$$

Therefore, (5.12) describes an initial condition very similar to that described by (5.1), but the form of (5.10) is more tractable to analysis, and will be the velocity perturbation to be analysed from here on.

The initial conditions for the density perturbation in this case are,

$$\rho' = 0, \tag{5.14}$$

$$\frac{\partial \rho'}{\partial t} = -\frac{\mathrm{d}\rho_0}{\mathrm{d}z}\frac{\Gamma_0}{2\pi r}\cos\theta[1 - e^{-(r/r_0^2)}], \tag{5.15}$$

and (2.4) yields the results,

$$\frac{\rho'(\mathbf{r}, t)}{\rho_0} = -\frac{\Gamma_0 N}{4\pi g}\int_0^\infty e^{-k^2 r_0^2}[J_0(L^+) - J_0(L^-)]\,\mathrm{d}k, \tag{5.16}$$

where $L^\pm$ is defined in §3.

The expression (5.16) can be evaluated by using (4.5) and relation 11.4.28 in HMF to obtain the following exact solution.

$$\frac{\rho'(\boldsymbol{r},t)}{\rho_0} = \frac{\Gamma_0 N}{\pi g r_0} \sum_{l=0}^{\infty} \frac{\Gamma(l+1)}{\Gamma(2l+2)} \left(\frac{r}{r_0}\right)^{2l+1} \cos\left[(2l+1)\theta\right] J_{2l+1}(Nt)\, M\left[l+1, 2l+2, -\left(\frac{r}{r_0}\right)^2\right]. \tag{5.17}$$

Similarly, for the vorticity, we find

$$\Omega = \frac{\Gamma_0}{\pi r_0^2}\left\{ e^{-r^2/r_0^2} J_0(Nt) + 2 \sum_{l=1}^{\infty} \frac{\Gamma(l+1)}{\Gamma(2l+1)} \left(\frac{r}{r_0}\right)^{2l} \cos(2l\theta) J_{2l}(Nt)\, M\left[l+1, 2l+1, -\left(\frac{r}{r_0}\right)^2\right]\right\}. \tag{5.18}$$

The asymptotic expression for (5.17), as $r/r_0 \to \infty$ can be obtained by invoking the asymptotic formula for the confluent hypergeometric function, 13.1.5 in HMF. The result is found to be identical to the asymptotic form of the modified Rankine vortex model, namely, (5.8). This is expected since the far-field amplitude generated by a vortex does not depend upon the detailed local flow at the source, it only depends upon the overall characteristics of the vortex. Similarly, the asymptotic result for the vorticity is found to be identical to (5.9).

The stationary phase result can be shown to be

$$\frac{\rho'}{\rho} \sim \frac{\Gamma_0 N}{2\pi g r} e^{-(Ntr_0 \cos\theta/r)^2} \cos(Nt \sin\theta), \tag{5.19}$$

which decays slower than both the smoothed density and swirl cases. Along the ray $Nt \sin\theta = kr$, so that the above equation can be reduced to

$$\left.\frac{\rho'}{\rho}\right|_{\text{ray}} \sim \frac{\Gamma_0 N}{2\pi g r} e^{-(kr_0 \cot\theta/r)^2} \cos(kr), \tag{5.20}$$

which obviously has a maximum at $\theta = \frac{1}{2}\pi$, i.e. the most energetic rays are vertical. This difference will be clearly illustrated in the contour plots.

5.5. *Comparison with finite-difference solution*

The results of the previous sections are compared with the outputs of a finite-difference computer code that solves the fully nonlinear Navier–Stokes equations in the Boussinesq approximation. This comparison is useful in establishing the range of vortex velocity perturbations over which the linear approximation is accurate.

The vortex model of §5.4 was selected for this comparison. The density-contour plots obtained from a numerical evaluation of (5.17), using the technique described in §5.3, are very similar to figure 7, given the same flow conditions. It is clear from these figures that the flow for these values of the flow parameters is not in the linear regime. The input conditions, which were found to give a linear flow, yield the following non-dimensional parameters:

$$F_{\text{vorticity}} = \frac{\Gamma_0}{N r_0^2} = 5.0, \quad F_{\text{vortex}} = \frac{\Gamma_0}{\pi N b^2} = 0.0442, \quad \tilde{g} = \frac{g r_0^3}{\Gamma_0^2} = 39.20,$$

which is essentially a factor of ten reduction in Γ_0 from the results shown in figure 7. A computational domain of dimensions $20D$ in the horizontal direction and $20D$ in the vertical direction was found to be sufficiently large to minimize the effects of the

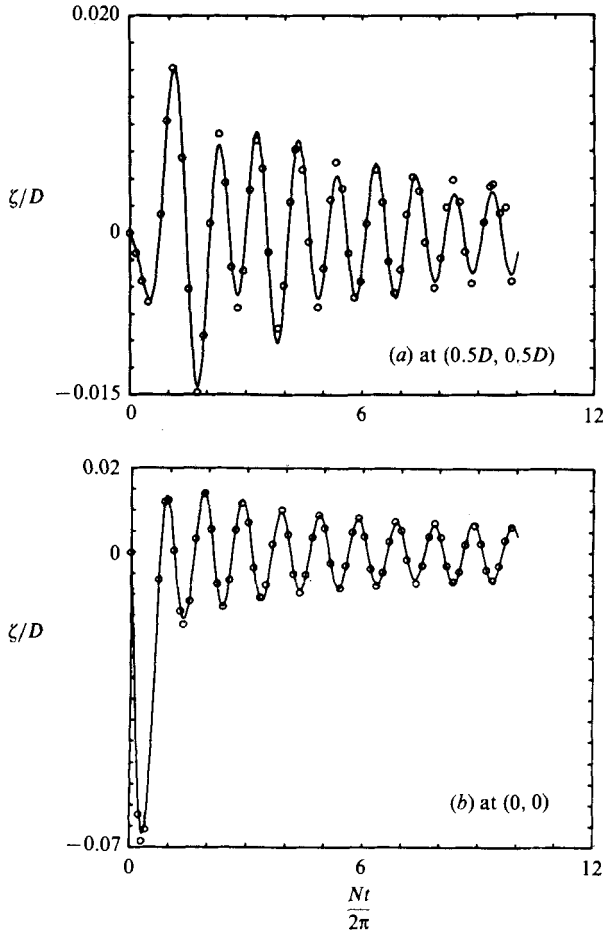

FIGURE 8. The isopycnic displacements vs. B.V. period at two positions of the computational plane for the vortex pair case. ——, numerical solution of the fully nonlinear Navier–Stokes equations; ○, linear theory.

solid walls in the region of interest. The symmetry of the flow was used so that only half of the flow field was actually computed.

Plots comparing the results of the two calculations in terms of the history of the isopycnic displacements at three near-field locations on the computational plane are presented in figure 8(*a*, *b*). The centre between the vortices is located at the origin of the coordinate system on the computational plane. Like the previous two cases, fluid at all three locations oscillates at a frequency close to the B.V. frequency. The agreement between the analytic results and finite-difference results is remarkably good. Note that after the initial impulse, the envelopes of these curves assume the predicted $(Nt)^{-\frac{1}{2}}$ asymptotic behaviour.

Figure 9 shows the history of the potential energy per unit length on the computational plane as computed by the finite-difference code. It is remarkable that half of the initial kinetic energy is converted into potential energy at 0.15 B.V. periods: a more efficient conversion of the energies than both the smoothed density perturbation and swirl-flow cases. Again, like the other two cases, the vortex flow reaches an equi-partitioning of energy at 0.4 B.V. periods. After the initial impulse,

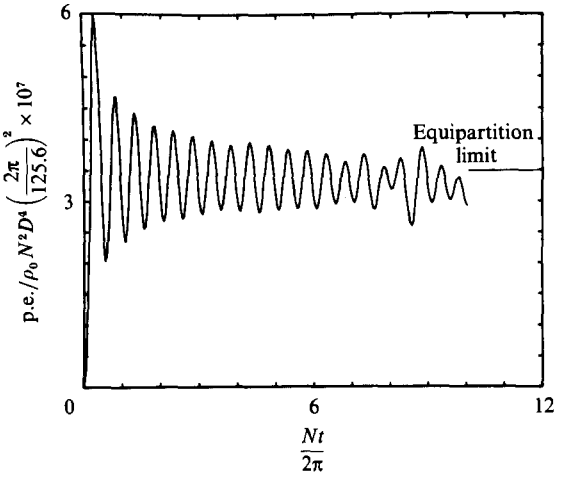

FIGURE 9. The potential energy per unit lenth on the computational plane vs. B.V. period for the vortex pair case.

the potential energy is constant, on average, and the influence of wave reflection is seen beginning at $Nt = 7.16$ cycle.

6. Conclusion

A generalized theoretical analysis of the initial-value problem is applied to obtain the linear internal wave fields generated by a density perturbation and two rotational velocity perturbations in an inviscid linearly stratified fluid. The velocity perturbations are those due to an axisymmetric swirl and a vortex pair. Our results correspond to the weak rotational flows or equivalently for a strongly stratified fluid. The solution for a smoothed version of the discontinuous density perturbation used by HL is also obtained. For the vortex case, two representations were applied: one is the modified Rankine model and the other is the Lamb model. Solutions are given in closed form for the density deviation from the ambient density, the stream function and the vorticity. Asymptotic expressions for both the long-time and far-field limits are established. The stationary phase results and the most energetic ray angles are derived and intercompared. The key differences and similarities of the internal wave amplitude are best illustrated in tabulated form and are shown in table 1.

Comparison of the result of the smoothed density-perturbation case with the results obtained by HL, for the same initial potential energy, shows that our result is a factor of four higher in the internal-wave amplitude in the far field. This is because in the discontinuous case, a portion of the total energy is 'trapped' at $r = a$ where the fluid oscillates persistently, as described by HL, and does not radiate to the far field; while in our smoothed case no energy is trapped. The amount of energy trapped in HL's discontinuous case accounts for the smaller far-field amplitude.

The theoretical results of the stream function and vorticity show that the rotational perturbation cases possess an oscillating non-propagating disturbance, decaying slowly in proportion to $J_0(Nt)$, which is absent in the density-perturbation case. Therefore the near fields of the velocity-perturbation cases are dominated by their initial vorticity which are clearly shown in the density contour plots. The swirl-

Characteristics: initial conditions	Most energetic ray angle θ from horizontal	Decay rate along ray	Far field decay law	Long time decay law	Time needed for conversion of half of initial energy
Smoothed density	$\tan\theta = \frac{kr_0}{\sqrt{6}}$	r^{-2}	r^{-3}	$(Nt)^{-\frac{3}{2}}$	P.E. → K.E. 0.33 B.V. period
Swirl	$\tan\theta = \frac{kr_0}{2\sqrt{2}}$	r^{-1}	r^{-3}	$(Nt)^{-\frac{1}{2}}$	K.E. → P.E. 0.25 B.V. period
Vortex	$\theta = \frac{1}{2}\pi$	r^{-1}	r^{-1}	$(Nt)^{-\frac{1}{2}}$	K.E. → P.E. 0.15 B.V. period

TABLE 1

flow solution shows an oscillatory behaviour in both the angular momentum deposited in the fluid and in the torque exerted by the external gravitational force field. Both of them oscillate at a frequency slower than but asymptotically approaching the B.V. frequency. They are nearly 90° out of phase from each other. This can be called a 'torsional pendulum' in analogy to its counterpart in solid mechanics. Comparing the asymptotic expressions of the two vortex models, i.e. Rankine's and Lamb's, we find that they are identical, confirming the intuition that the far-field solutions do not depend upon the detailed local flow at the source, i.e. (5.1) versus (5.10); it only depends upon the overall characteristics of the vortices.

The analytical solutions in terms of the infinite series are evaluated numerically for all three cases and are presented in the form of density contour plots as a function of time. These near-field contour plots reveal that the fundamental difference between the internal wave field generated by a density perturbation and one generated by velocity perturbation is that the velocity perturbations possess a non-propagating vorticity field mentioned above.

Finite-difference solutions of the Navier–Stokes equations are also obtained for all three perturbations. The results are presented in terms of isopycnic displacements versus B.V. period at several near-field locations. They all show oscillations at frequencies close to the B.V. frequency. They are compared with the linear theoretical solutions, and excellent agreement between them is found for all cases. By this comparison, we also found the linear limits for the swirl and vortex cases, expressed in terms of the Froude numbers, to be $F_{\text{swirl}} \approx 1.7$ and $F_{\text{vortex}} \approx 0.04$. Histories of the energies are also obtained from the finite-difference solutions. In the linear limit, the equi-partitioning of energy is reached at about 0.4 of a B.V. period. The potential energy–kinetic energy conversion, or vice versa, takes place between 0.15 to 0.3 B.V. periods, with the vortex-pair flow, among the three cases studied, being the most efficient one.

This work was performed under the technical supervision of Applied Physics Laboratory, The Johns Hopkins University, and was supported by Navy Contract No. N00017-72-C-4401. The work was complated in 1977 when both authors were at Science Applications, Inc., La Jolla, California, and was revised and submitted for publication by the senior author in 1985. The authors wish to acknowledge many helpful suggestions from Drs H. E. Gilreath and L. Cronvich at APL/JHU and support in computer graphics from Mr G. E. Innis at Science Applications, Inc.

REFERENCES

ABRAMOWITZ, M. & STEGUN, I. A. 1972 *Handbook of Mathematical Functions* (10th edn). National Bureau of Standards.

BROWN, C. E. & KIRKMAN, K. 1974 Simulation of wake vortices descending in a stably stratified atmosphere. *Rep.* FAA-RD-74-116.

CHAN, R. K. C. 1977 Second International Conference on Numerical Ship Hydrodynamics (ed. J. V. Wehausen & N. Salvesen), pp. 39–52. University Extension Publications, University of California at Berkeley.

ERDELYI, A. 1953 *Higher Transcendental Functions*, vol. 1. McGraw-Hill.

HAN, T. Y., MENG, J. C. S. & INNIS, G. E. 1983 An open boundary condition for incompressible stratified flows. *J. Comp. Phys.* **49**, pp. 276–297.

HARLOW, F. H. & WELCH, J. E. 1965 Numerical calculation of time-dependent viscous incompressible flow. *Phys. Fluids* **8**, 2182.

HARTMAN, R. J. & LEWIS, H. W. 1972 Wake collapse in a stratified fluid: linear treatment. *J. Fluid Mech.* **51**, 613–618.

HILL, F. M. 1975 A numerical study of the descent of a vortex pair in a stably stratified atmosphere. *J. Fluid Mech.* **71**, 1–13.

JANOWITZ, G. S. 1968 On wakes in stratified fluids. *J. Fluid Mech.* **33**, 417–432.

LIGHTHILL, J. 1978 *Waves in Fluids*. Cambridge University Press.

LIN, J. T. & PAO, Y. H. 1979 Wakes in stratified fluids. *Ann. Rev. Fluid Mech.* **11**, 317–338.

MEI, C. C. 1969 Collapse of a homogeneous fluid mass in a stratified fluid. *12th Intl Congr. Appl. Mech.* pp. 321–330. Springer.

MILES, J. W. 1971 Internal waves generated by a horizontally moving source. *Geophys. Fluid Dyn.* **2**, 63.

MILNE-THOMSON, L. M. 1968 *Theoretical Aerodynamics*. Macmillan.

PEYRET, R. 1976 Unsteady evolution of a horizontal jet in a stratified fluid. *J. Fluid Mech.* **78**, 49–63.

SAFFMAN, P. G. 1972 The motion of a vortex pair in a stratified atmosphere. *Stud. Appl. Maths* **21**, 107–119.

SCHOOLEY, A. & HUGHES, B. A. 1972 An experimental and theoretical study of internal waves generated by the collapse of a two-dimensional mixed region in a density gradient. *J. Fluid Mech.* **51**, 159–175.

SCHOOLEY, A. & STEWART, R. W. 1963 Experiments with a self-propelled body submerged in a fluid with a vertical density gradient. *J. Fluid Mech.* **15**, 83–96.

TOMBACH, I. 1974 The effects of atmospheric stability, turbulence, and wind shear on aircraft wake behavior. *Sixth Conf. on Aerospace and Aeronautical Meteorology of the Am. Met. Soc. Nov. 12–15, El Paso, Texas*, pp. 405–411.

WATSON, G. N. 1958 *A Treatise on the Theory of Bessel Functions*. Cambridge University Press.

WESSEL, W. R. 1969 Numerical study of the collapse of a perturbation in an infinite density stratified fluid. *Phys. Fluids Suppl.* **2**, 11–171.

WU, J. 1969 Mixed region collapse with internal wave generation in a density-stratified medium. *J. Fluid Mech.* **35**, 531–544.